PAPER

Check for updates

Dopamine detection using leaf-shaped ZnO synthesized from zinc shells of recycled batteries

Md Yeasin Pabel,[a] Md Humayun Kabir, ![ID] *[a] Md. Sanwar Hossain,[a] Fahima Mojumder,[a] Sourav Datta,[a] Muhammad Shahriar Bashar[b] and Sabina Yasmin ![ID] *[a]

This study presents a cost-effective and sustainable method for synthesizing ZnO from electronic waste (e-waste) for the electrochemical detection of dopamine (DA) using a single metal oxide. The purity and various properties of the ZnO were confirmed using advanced techniques. The growth of ZnO clusters along the [0001] direction results in the formation of leaf-shaped ZnO with a direct band gap of 3.27 eV. Cyclic voltammetry, differential pulse voltammetry, and amperometric studies demonstrated successful DA detection at the ZnO–glassy carbon electrode in aqueous media, with an equal number of electron and proton pathways for DA oxidation. The sensor exhibited a linear response over a wide concentration range (0.01 to 100 μM), with a low limit of detection of 0.47 nM and a high sensitivity of 0.0389 A M^{-1}. Additionally, the sensor showed high selectivity, repeatability and reproducibility with relative standard deviation of 4.80% in DA detection and proved effective in real sample analysis. These results suggest that the developed sensor holds great potential as a sensitive, practical, and cost-efficient tool for DA monitoring. Furthermore, the approach contributes to sustainable management of zinc–carbon battery waste by producing valuable ZnO.

1. Introduction

3,4-Dihydroxyphenethylamine, also known as dopamine (DA) and often referred to as the happiness molecule, functions as a neurotransmitter in the brain and nervous system, playing a vital role in regulating mood, motivation, reward, and motor control, playing a crucial role in various biological processes related to emotions and perception.[1–3] Imbalances in DA levels in the blood serum are associated with diseases such as schizophrenia (excessive DA) and Parkinson's disease (deficient DA).[4–6] While these diseases are incurable, early detection can facilitate management.[5] Therefore, there is a pressing need for sensitive and selective detection of DA accurately for medical diagnosis. Among the various methods for DA detection, the electrochemical technique has gained popularity in sensing applications due to its numerous advantages, including ease of operation, real-time detection, and high sensitivity and selectivity. However, realizing these benefits relies on selecting suitable materials for modifying substrate electrodes.[7–10] While many proposed sensors rely on composite materials for their

synergistic properties,[11–15] these often face challenges such as complex synthesis procedures and inconsistent material homogeneity, which can compromise sensor reliability and performance.[16,17] In contrast, single metal oxides offer a simpler composition, ensuring greater reproducibility and uniformity in sensor performance—key factors for precise and consistent DA detection. Additionally, single metal oxides are typically more cost-effective and easier to fabricate, as they eliminate the need for intricate blending or multi-step preparation processes.[18–20] These attributes make single metal oxides an attractive alternative for the development of efficient and reliable electrochemical sensors.

In the digital era, electronic waste (e-waste) has become a critical environmental issue,[21,22] with zinc–carbon batteries (ZCBs) being significant contributors due to their widespread use and inadequate disposal.[23] However, their improper disposal exacerbates landfill congestion and environmental pollution, posing severe health and ecological risks.[24,25] Addressing these challenges, sustainable solutions for ZCB recycling have gained attention, including extracting graphite, manganese oxides, and zinc for reuse.[22,23,26,27] ZCB consists of a graphite positive electrode surrounded by manganese dioxide and carbon powder, encased within a zinc container acting as both packaging and a negative electrode.[23,26] Graphite from spent ZCBs has been successfully repurposed for graphene-based materials,[28–32] while zinc recovery efforts have focused on

[a] *Institute of National Analytical Research and Service (INARS), Bangladesh Council of Scientific and Industrial Research (BCSIR), Dhanmondi, Dhaka-1205, Bangladesh. E-mail: humayunkabir@bcsir.gov.bd, sabinayasmin@bcsir.gov.bd*

[b] *Institute of Energy Research & Development (IERD), Bangladesh Council of Scientific and Industrial Research (BCSIR), Dhanmondi, Dhaka-1205, Bangladesh*

producing low-cost ZnO. Therefore, extracting zinc from waste ZCBs presents a sustainable and cost-effective alternative, addressing resource limitations while enhancing waste management and reducing environmental impact.

Recycling methods for e-waste primarily include pyrometallurgy, which uses high temperatures to extract metals but involves high energy consumption and environmental risks, and hydrometallurgy, which dissolves metals in chemical solutions but generates substantial waste requiring careful management.[23,27] To address these limitations, simpler and more sustainable approaches for ZnO synthesis from e-waste-derived Zn are necessary. Here, we propose a straightforward precipitation method for synthesizing highly pure ZnO using zinc hulls recovered from discarded ZCBs. This approach offers a simple, cost-effective, and environmentally friendly solution for recycling e-waste while producing valuable ZnO.

In this study, we present a simple and efficient precipitation method to synthesize highly pure ZnO from zinc hulls recovered from discarded ZCBs for use as a sensitive and selective electrochemical sensor for DA. This approach minimizes energy consumption and environmental impact compared to conventional zinc extraction methods while enabling the development of single metal oxide-based electrochemical detectors for DA sensing. This method not only mitigates the environmental burden of e-waste but also transforms waste materials into valuable products such as ZnO, which hold economic potential for sensor applications and beyond.
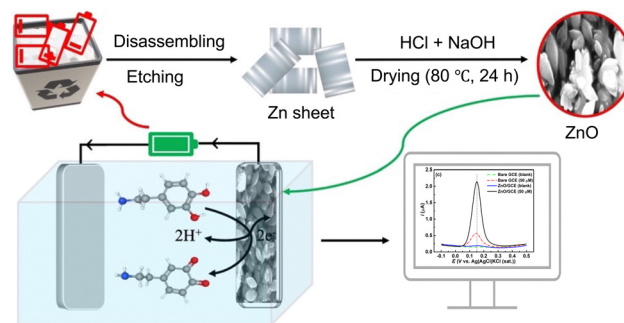
2. Experimental

2.1. Reagents and chemicals

Analytical grade DA, uric acid, 4-nitrophenol, glucose, HCl, NaOH and other chemicals were purchased from Sigma-Aldrich (Merck), Germany. All chemicals were used as received, without further purification. Ultrapure deionized water (DI) (18 MΩ·cm) was used to prepare all solutions.

2.2. Instruments

The morphology of the samples was analyzed using scanning electron microscopy (SEM) (EVO18, Carl Zeiss AG, Germany) at various magnifications with a 15 kV electron beam voltage. Elemental composition was determined by energy-dispersive X-ray spectroscopy (EDS) (TEAM EDS; EDAX, USA). The Fourier-transform infrared (FTIR) spectrum was acquired in transmittance mode using a PerkinElmer Frontier spectrophotometer (USA). X-ray diffraction (XRD) patterns were recorded with a Thermo Scientific ARL Equinox diffractometer (Cu Kα1, λ = 1.5406 Å, 40 kV, 30 mA). Ultraviolet-visible (UV-Vis) diffuse reflectance spectra were measured with a Shimadzu UV-1800 spectrophotometer (Japan) to determine the optical band gap (E_g). Photoluminescence (PL) spectra were obtained using a Hitachi F-7000 spectrophotometer with a 150 W xenon lamp at room temperature. Electrochemical analyses were performed using a CHI660 device (USA) with a glassy carbon (GC) working

Scheme 1 Synthesis of ZnO nanostructures and their application in DA detection. (Upper panel) Schematic representation of the synthesis of ZnO nanostructures from waste batteries. (Lower panel) Electrochemical detection of DA using the ZnO-based electrode.

electrode (Φ = 3 mm), Ag/AgCl/KCl (sat.) reference electrode, and a spiral Pt wire counter electrode.

2.3. Recovery of Zn–metal and synthesis of ZnO

To preserve the integrity of the Zn shell, the waste batteries were carefully dismantled. The Zn shell was then cleaned with deionized water to remove the attached mixture of MnO$_2$, NH$_4$Cl, carbon powder, and other substances. The Zn metal was polished using sandpaper and cleaned with Triton X-100 surfactant to remove impurities, resulting in a shiny surface. The Zn metal was dissolved in concentrated HCl, and 1 M NaOH was gradually added until Zn(OH)$_2$ precipitated (Scheme 1). The product was separated via centrifugation, rinsed multiple times with DI water until the pH reached 7, and then washed with ethanol to remove any organic residue. Finally, the ZnO product was dried in a vacuum oven for 24 hours at 80 °C.

2.4. Fabrication of the ZnO modified GC electrode

The GC electrode (CHI104, Φ = 3 mm) was meticulously polished using a polishing microcloth and an aqueous slurry of fine alumina particles. After polishing, the GC electrode was subjected to 5 minutes of ultrasonication in deionized water to remove any remaining alumina particles. The prepared ZnO was fully suspended in deionized water at a concentration of 1 mg mL^{-1} using sonication. A homogeneous suspension was then drop-cast onto the GC electrode, and the electrode was allowed to dry at room temperature, forming a uniform film of active components. This modified electrode was used for subsequent electrochemical measurements.

3. Results and discussion

3.1. Characterization

3.1.1. **Functional group and structural analysis.** Fig. 1A presents the FTIR spectrum of ZnO, showing distinct bands corresponding to ZnO. The bands at 425 and 891 cm^{-1} are specifically attributed to the stretching and bending vibrations of the Zn–O bond in ZnO.[33,34] It is well known that Zn–O stretching vibration is in the range of 400 to 600 cm^{-1}.[33–36]
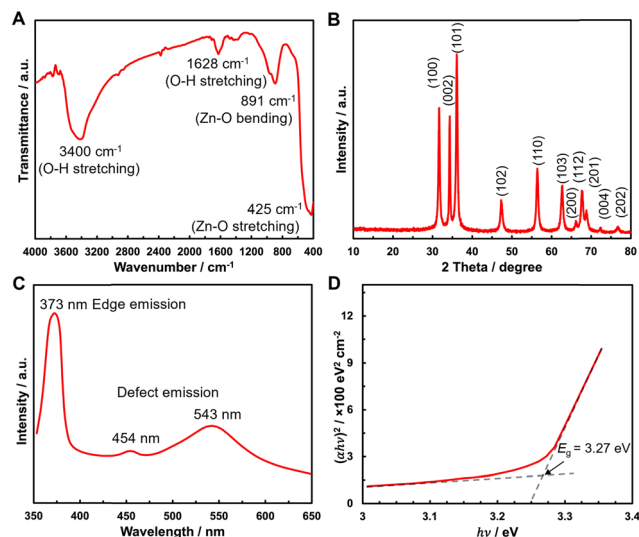
Fig. 1 Structural and optical characterization of ZnO. (A) FTIR spectrum showing the functional groups present. (B) XRD pattern with labeled peaks corresponding to specific crystalline planes. (C) PL spectrum indicating the optical emission properties. (D) Tauc plot showing the optical bandgap energy derived from UV-Vis absorption data. The dotted lines in the Tauc plot indicate the base (horizontal) and fitted (vertical) lines. a.u. on the *Y*-axes indicates arbitrary units.

Additionally, the presence of –OH groups on the ZnO surface was observed (Fig. 1A). These –OH groups likely originated from chemisorbed and/or physisorbed water molecules during FTIR analysis, as the successful conversion of $Zn(OH)_2$ to ZnO was confirmed through XRD and EDS spectra (Fig. 1B and 2D). Furthermore, the morphological analysis discussed in Section 3.1.3 suggested possible reactions involved in ZnO synthesis (Scheme 2A).
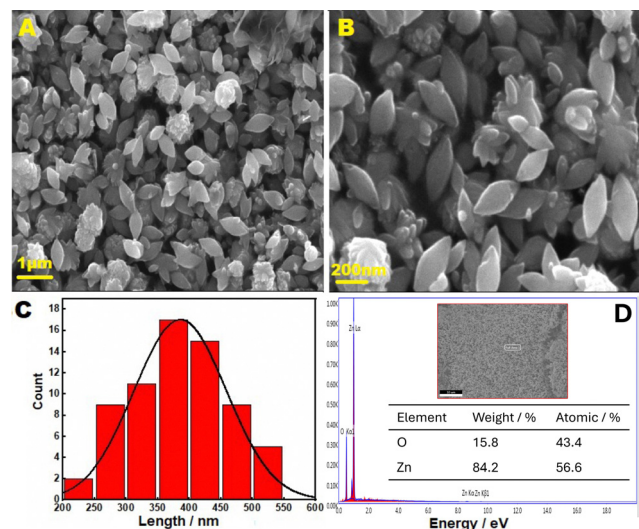

Fig. 2 Morphological and compositional analysis of ZnO. (A) and (B) SEM images at two different magnifications. (C) Particle size distribution histogram derived from the SEM image (B), with a Gaussian fit shown as a black curve. (D) EDS spectrum, with the inset showing the full area analyzed (upper) and the elemental composition (lower).

Then, dried ZnO particles were subjected to XRD analysis using Cu-K$_\alpha$ radiation (λ = 1.54060 Å), with relative intensity data collected over a 2θ range of 10–80° (Fig. 2B). The XRD pattern of ZnO exhibits sharp and intense peaks, indicative of the high purity and crystallinity of the synthesized ZnO (Fig. 2B). The diffraction bands at 2θ of 31.70°, 34.32°, 36.15°, 47.33°, 56.36°, 62.71°, 65.98°, 67.77°, 68.79°, 72.57°, and 76.85° correspond to the (100), (002), (101), (102), (110), (103), (200), (112), (201), (004), and (202) planes of the hexagonal wurtzite ZnO lattice.[33–38] Importantly, no additional diffraction peaks were observed, indicating the purity of ZnO. The absence of characteristic peaks of $Zn(OH)_2$, such as those at $\sim$19.0°, 35.6°, and 53.1°, further confirms the complete conversion of $Zn(OH)_2$ to ZnO.[39,40] Faisal *et al.* also reported that thermal treatment during the synthesis of ZnO facilitates the conversion of $Zn(OH)_2$ to high-purity ZnO.[36] Therefore, this evidence suggests the successful conversion of $Zn(OH)_2$ to ZnO.

3.1.2. Optical properties. PL spectroscopy is a very effective method for investigating the impact of morphology on the optoelectrical characteristics of semiconductor materials like ZnO.[41–43] Fig. 1C displays the PL spectrum of the synthesized ZnO, revealing three distinct emission bands. One of these bands corresponds to UV edge emission, while the other two bands correspond to visible light emission and are associated with the defects present in the manufactured ZnO.[42,43] The presence of a distinct and intense emission peak at a wavelength of 373 nm can be attributed to the recombination of electrons and holes, which is commonly referred to as UV band edge emission.[42,43] Typically, this band is located at a wavelength of around 385 nm.[43] The observed shift of the emission band towards shorter wavelengths suggests an increase in the optical band gap, a phenomenon known as the Moss–Burstein effect.[41,43] The Moss–Burstein effect states that the optical band gap of a semiconductor system grows as the number of free electrons in the system increases.[41] The emissions at a wavelength of 454 and 543 nm are mostly caused by defects in the ZnO nanomaterial, such as oxygen vacancies or interstitial zinc ions.[42,43]
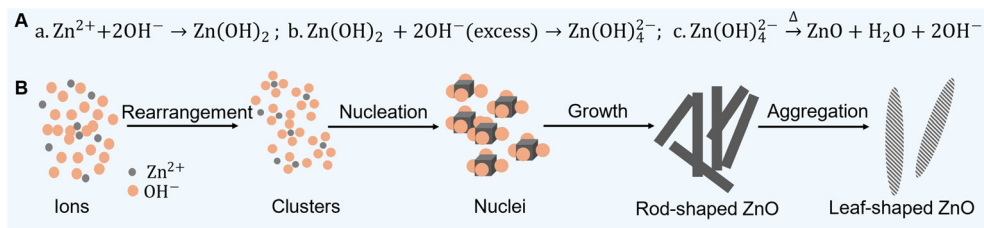
The optical band gap value of the produced ZnO was determined by calculating the absorption energy associated with the electron excitation from the valence band to the conduction band, as seen in Fig. 1D. The band gap energy was calculated using eqn (1) based on the Tauc plot (Fig. 1D).[44]

$$(\alpha h \nu)^{1/n} = A(h\nu - E_g) \tag{1}$$

where α, $h\nu$, and A are the absorption coefficient, the photon energy, and the constant exponent related to the type of transition that occurs in the material, respectively. The values of n, which might be 1/2, 2, 3/2, and 3, correspond to allowed indirect, direct, prohibited indirect, and forbidden direct transitions, respectively.[44,45] The prepared ZnO has a direct band gap energy value of 3.27 eV, which aligns with findings from prior studies.[45]

3.1.3. Surface morphology and elemental analysis. The shape and microstructure of the synthesized ZnO were assessed by analyzing the SEM images (Fig. 2A and B). The ZnO exhibited

Scheme 2 Reactions and mechanisms in ZnO formation. (A) Possible reactions involved in the synthesis of ZnO. (B) Proposed mechanism for the formation of ZnO leaf structures.

a leaf-shaped morphology that was evenly distributed (Fig. 2A and B). However, another particle form, resembling a cauliflower, was also observed. This leaf-shaped morphology of ZnO may enhance its surface area and ability to interact with dopamine (see Section 3.2.1). Fig. 2C displays the particle size distribution obtained from the SEM images using ImageJ software (64-bit). The average particle length measured approximately 385 nm. The EDS spectrum of ZnO in Fig. 2D revealed its elemental composition. The prepared ZnO consisted of 15.8% oxygen and 84.2% zinc by weight, with atomic percentages of 43.4% and 56.6%, respectively (Fig. 2D). The absence of additional peaks in the EDS spectrum indicates the high purity of the prepared ZnO.

The morphology of ZnO is influenced by a combination of kinetic factors, such as the growth rates of different crystal surfaces, and thermodynamic factors, which relate to the energetic stability of the overall structure.[46–52] ZnO can form a wide range of morphologies, including nanorods, needles, leaf, flower, tubes, belts, wires, combs, *etc.*, depending on the nature of the solvent, precursor materials, reaction temperature, reaction duration, and solution pH.[36,46,50–52] In this study, Zn metal collected from a Zn–C battery was dissolved in concentrated HCl, and 1.0 M NaOH was gradually added until $Zn(OH)_2$ precipitated. The precipitate was then dried in a vacuum oven for 24 hours at 80 °C (Scheme 1). The possible reactions involved in ZnO formation and a plausible mechanism for the formation of leaf-like ZnO are shown in Scheme 2.

Generally, the excessive addition of NaOH to Zn^{2+} leads to the formation of zincate ions $(Zn(OH)_4^{2-})$, which undergo dehydration upon heating to produce ZnO[36] (Scheme 2A). As the solution is heated, the ions rearrange to form clusters and generate stable nuclei (Scheme 2B). The direction of growth of these nanostructures depends on the selective adsorption effect on certain facets. The presence of excess OH^- generally promotes the growth of ZnO clusters along the [0001] direction, resulting in rod-shaped ZnO[36] (Scheme 2B). The leaf-like structures are formed as multiple nanorods come together in an ordered array. This aggregation is driven by thermodynamic stability, where larger leaf-shaped structures are energetically more favorable than smaller nanorods.

3.2. Electrochemical dopamine sensing

3.2.1. Electrochemical activity of ZnO/GC for DA oxidation. The electrochemical sensor activity of the ZnO/GC electrode for DA oxidation was evaluated by cyclic voltammetry and differential pulse voltammetry using a standard three electrode system in 0.1 M PBS (pH 6.9) containing 50 µM DA. Fig. 3A shows the cyclic voltammograms (CVs) recorded at bare GC and ZnO/GC electrodes in the absence and presence of DA. Without DA, neither electrode exhibited discernible faradaic currents, confirming the absence of non-specific redox activity (Fig. 3A). Conversely, upon DA introduction, well-defined anodic and cathodic peaks emerged at both electrodes, signifying the characteristic redox behavior of DA. Notably, the anodic peak
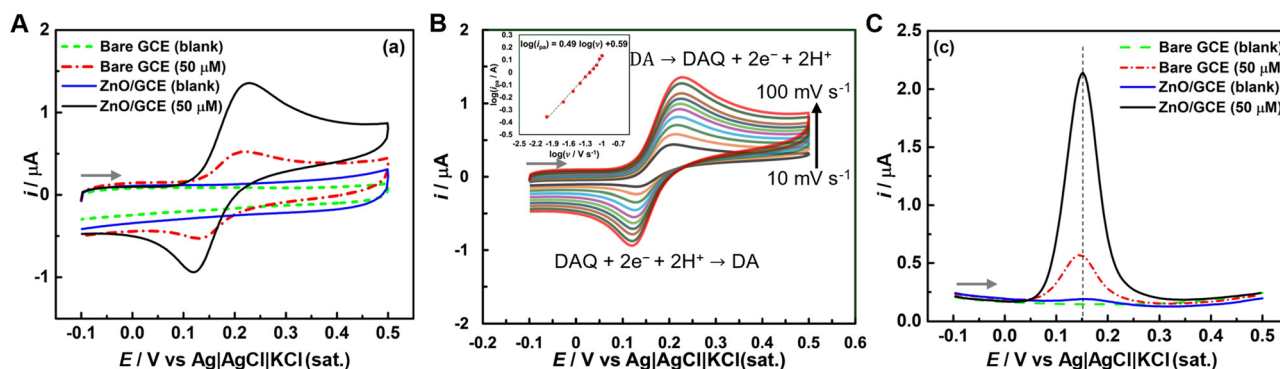

Fig. 3 Electrochemical characterization of the ZnO/GC electrode for DA detection in 0.1 M PBS. (A) CVs recorded at bare GC and ZnO/GC electrodes in the absence and presence of DA at a scan rate of 100 mV s⁻¹. (B) CVs at the ZnO/GC electrode in the presence of DA at various scan rates. DA and DAQ denote dopamine and dopaminequinone, respectively. Inset: Logarithmic plot of anodic peak current *versus* logarithm of scan rate with the fitted equation. (C) DPVs at GC and ZnO/GC electrodes in the absence and presence of DA. The horizontal array indicates the initial scan direction. The experimental parameters for DPV: potential increment = 4 mV, pulse amplitude = 50 mV, pulse width = 60 ms, and pulse period = 0.5 s.

current at the ZnO/GC electrode exhibited a nearly threefold enhancement relative to that of the bare GC electrode, indicating the superior electrocatalytic efficacy of the leaf-shaped ZnO in facilitating DA oxidation. Fig. 3B displays the CVs at the ZnO/GC electrode in the presence of DA at various scan rates. As the scan rate increases, the peak current of the oxidation and reduction also increases, as expected. The logarithm of oxidation peak current against the logarithm of scan rate showed a strong relationship with a slope of 0.49 (inset of Fig. 3B). This value is very close to the theoretical slope of 0.5, characteristic of a diffusion-controlled faradaic process. On the other hand, the reduction peak current showed a linear relationship with the scan rate, suggesting that the reduction of oxidized DA at the ZnO/GC electrode is predominantly governed by adsorption processes.

Fig. 3C shows the differential pulse voltammograms (DPVs) obtained at bare GC and ZnO/GC electrodes in the absence and presence of DA. Like CVs, no oxidation peak was detected in the absence of DA at either electrode (Fig. 3C). However, in the presence of DA, both electrodes displayed oxidation peaks corresponding to DA oxidation. The peak potential (E_p) at the ZnO/GC electrode was slightly shifted towards a more positive potential, and the peak current (i_p) at the ZnO/GC electrode was *ca.* 4.5 times greater than that at the GC electrode. This significant increase in oxidation current at the ZnO/GC electrode compared to the GC electrode highlights again the superior electrocatalytic activity of the ZnO/GCE for DA sensing. The electrochemically active surface area (ECSA) of the ZnO/GC electrode was evaluated using the Randles–Sevcik equation in a standard ferri/ferrocyanide redox couple solution. The ECSA of the ZnO/GC electrode was determined to be *ca.* 2.1 times greater than the geometric surface area of the bare GC electrode (0.0707 cm^2). Therefore, the substantial enhancement in the i_p at the ZnO/GC electrode can be attributed to the increased ECSA of the modified electrode and the improved interaction between the ZnO and DA molecules, leading to greater DA accumulation on the electrode.

Fig. 4A presents DPVs for electrochemical DA sensing in PBS solution at various pHs using a ZnO/GC electrode. Shifts in peak potential and changes in peak current intensity for DA oxidation were observed with the pH medium (Fig. 4A and B). At lower pH, peak currents are observed at more positive potentials, whereas at higher pH, the peaks shift to more negative potentials (Fig. 4A and B). This indicates that the oxidation potential and rate of oxidation of DA at the ZnO/GC electrode are pH dependent. In acidic conditions (pH = 3 to 6), DA is relatively stable, primarily existing in its protonated form.[53–57] As the pH increases to neutral and slightly basic levels (pH = 7 to 8), DA undergoes oxidation more easily, forming dopaminoquinone.[53,54,57] In basic conditions (pH = 9 to 11), oxidation is further favored, leading to the formation of various oxidized products, such as quinones, and potentially polymerization into melanin-like substances.[53,54,56] Consequently, DA is more susceptible to oxidation at higher pH levels, resulting in diverse chemical transformations. The E_p showed a linear relationship with the pH of the medium,
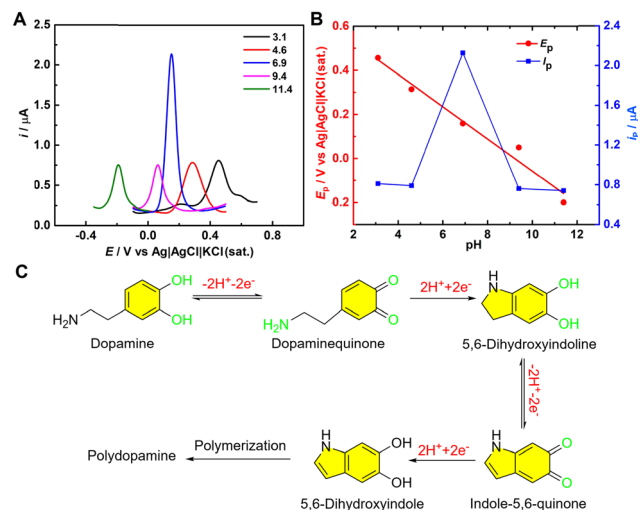

Fig. 4 pH-dependent DA oxidation at the ZnO/GC electrode in 0.1 M PBS. (A) DPVs in the presence of 50 μM DA at different pH values. (B) Plot of peak potential (E_p) versus pH and peak current (i_p) versus pH derived from (A). (C) Plausible mechanism for the electrochemical oxidation of DA at the ZnO/GC electrode. The experimental parameters for DPV: potential increment = 4 mV, pulse amplitude = 50 mV, pulse width = 60 ms, and pulse period = 0.5 s.

following the equation $E_p = 0.594–0.050$ pH (Fig. 4B). For a Nernstian reaction involving an equal number of protons and electrons, the expected slope of E_p versus pH is 59 mV pH^{-1}. The observed slope in this study (50 mV pH^{-1}), which is close to the theoretical value, suggests that an equal number of protons and electrons are involved in the oxidation of DA at the ZnO/GC electrode.

The highest peak current was observed at pH 6.9, indicating the optimal pH for DA oxidation at the ZnO/GC electrode. ZnO exhibits different surface dynamics in aqueous solutions across a broad pH range (3 to 11).[33–35,37,38] ZnO maintains surface stability and exhibits a positive surface charge in acidic conditions (pH 3 to 6), where DA exists in its protonated form. This results in a low oxidation rate (low peak current) due to coulombic repulsion between the like charges. At neutral to slightly basic pH (7 to 8), ZnO starts developing surface –OH groups,[35,37,38] resulting in higher current due to possible H-bonding between these hydroxyl groups and DA. Under basic conditions (pH 9 to 11), zincate ions ($Zn(OH)_4^{2-}$) are formed, which reduces the response to DA sensing.

A possible mechanism for the electrochemical oxidation of DA in PBS solution at the ZnO/GC electrode is illustrated in Fig. 4C. The cyclic voltammetric study indicated that the redox behavior of DA follows a quasi-reversible process, with electrooxidation being more favorable than reduction (Fig. 3A and B), which aligns with findings in the literature.[1,3,10,12] The oxidation process was diffusion-controlled (Fig. 3B) and involved an equal number of protons and electrons as discussed above. Typically, the electro-oxidation mechanism includes a two-step process where the two hydroxyl groups in DA are converted into dopaminequinone (Fig. 4C). This dopaminequinone is then transformed into 5,6-dihydroxyindole, which is further oxidized
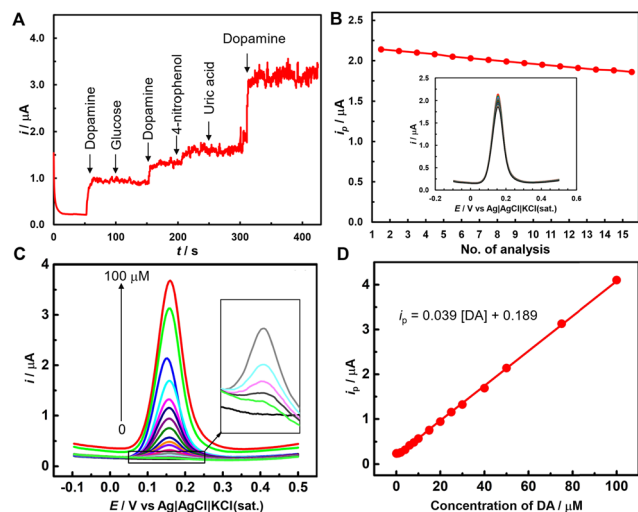
Fig. 5 Interference, repeatability, and quantitative analysis of DA at the ZnO/GC electrode in 0.1 M PBS. (A) amperometric response of 50 µM DA at 0.15 V in the presence of potential interfering species. (B) Plot of peak current *versus* analysis count from fifteen consecutive DPVs in a 50 µM DA solution, shown in the inset. (C) DPVs for varying DA concentrations (inset displays magnified DPVs for lower DA concentrations). (D) Calibration curve correlating peak current with dopamine concentration with the fitted equation derived from (C). The experimental parameters for DPV: potential increment = 4 mV, pulse amplitude = 50 mV, pulse width = 60 ms, and pulse period = 0.5 s.

to 5,6-dihydroxy indolyl quinone.[58] Repeated oxidation of DA ultimately leads to the formation of polydopamine, as shown in Fig. 4C.[58]

3.2.2. Interference, repeatability, and reproducibility. We employed the chronoamperometric technique at a potential of 0.15 V, the optimal potential for the oxidation of DA (Fig. 3), to assess the interference effects of various possible interfering substances (glucose, uric acid and 4-nitrophenol) towards the electrochemical selectivity of DA sensing.[8,59–61] Each interfering reagent was introduced at 50–60 s intervals for consistent

conditions and accurate response measurement. Initially, a distinct current spike followed DA addition, confirming successful oxidation of DA (Fig. 5A). Subsequently, introducing glucose resulted in no noticeable change in the current–time curve (Fig. 5A). This observation aligns with the higher potential required for the oxidation of glucose (around 0.4–0.6 V *vs.* SHE).[62–66] The re-introduction of DA again showed a clear signal, proving that the modified electrode responds specifically to DA (Fig. 5A). Neither 4-nitrophenol nor uric acid showed any chronoamperometric response at the ZnO/GC electrode (Fig. 5A). This lack of interference can be attributed to their higher oxidation potentials compared to DA. 4-Nitrophenol typically requires 0.1 to 0.3 V *vs.* SHE,[67,68] while uric acid needs 0.2 to 0.4 V *vs.* SHE[69,70] for oxidation. The final re-addition of DA resulted in a significant current response, confirming the reliability of the electrode (Fig. 5A). Notably, the ZnO/GC electrode showed no interference from uric acid, a common contaminant in biological samples. This indicates the potential use of the ZnO/GC electrode for selective DA detection in complex matrices.

For the repeatability study, fifteen consecutive DPVs were recorded at a ZnO/GC electrode in 50 µM DA in 0.1 M PBS (inset of Fig. 5B). Fig. 5B shows minimal variation in peak current with increasing analysis count, with only *ca.* 13% of the peak current dropped after the 15th experiment. The reproducibility of the ZnO/GC electrode was assessed through electroanalysis of 50 µM DA at three distinct ZnO/GC electrodes. The relative standard deviation (RSD) of the current responses recorded at the modified electrodes was 4.80%. Therefore, the repeatability and reproducibility studies demonstrated that the ZnO/GC electrode produced a consistent DA oxidation peak current.

3.2.3. Quantitative determination of DA. Fig. 5C presents the DPVs at the ZnO/GC electrode for DA concentrations from 0.01 to 100 µM in 0.1 M PBS at pH 6.9. The i_p increases linearly with DA concentration, following the calibration curve in Fig. 5D, again confirming the DA oxidation at the ZnO/GC electrode. The limit of detection (LOD) was calculated using the equation LOD = $3S/m$, where S represents the standard

Table 1 Comparative electrochemical performance of ZnO-based electrodes for DA detection in aqueous systems

Electrode	Method	Linear range (µM)	LOD (nM)	Ref.
GO–ZnO/GCE	DPV	1–70	330	9
ZnO/CF	DPV	6–20	402	14
Au–ZnO NCAs/GF	DPV	0–80	40	2
SPEEK/ZnO	SWV	5.4×10^{-7}–1.9×10^{-3}	0.89	71
ZnO/ErGO/GCE	SDLSV	0.01–80	3.6	10
Ti$_3$C$_2$/GMWCNTs/ZnO/GCE	DPV	0.01–30	3.2	11
N-ZnO/N-rGO	DPV	0.05–800	200	59
Ag–Cu@ZnO	Amperometry	0.1–10	210	60
3D-rGO–ZnO/GCE	DPV	0.01–70	0.06	8
ZnO–ZnFe$_2$O$_4$/Fe$_3$O$_4$/CN	DPV	0.01–61.34	1.57	61
ZnO@Au	DPV	0.1–500	86	72
ZnO/PC	DPV	0.10–100.0	22	73
β-Zn(OH)$_2$/ZnO	DPV	1.75–263 nM	0.17	74
In$_2$O$_3$ZnO@MC	Amperometry	0.5–2056	24	75
ZnO/GCE	DPV	0.01–100	0.47	This study

CF: nanofiber; CN: carbon nanocomposites; DA-CS: dopamine-imprinted chitosan film; ErGO: electro-reduced graphene oxide; GMWCNTs: graphitized multi-walled carbon nanotubes; MC: mesoporous carbon; MWCNTs: multi-walled carbon nanotubes; NCAs: nanocone arrays; P-rGO: porous reduced graphene oxide; PC: porous carbon; SDLSV: second derivative linear sweep voltammetry; SPEEK: sulphonated polyether etherketone; SWV: square wave votammetry; 3D-KSC: three-dimensional kenaf stem-derived macroporous carbon.

Table 2 Recovery of dopamine from real samples using the ZnO/GC-based electrochemical sensor

	Concentration of DA (μM)		
Sample no.	Added	Found	Recovery (%)
1	1.0	1.03 ± 0.05	103
2	2.0	2.14 ± 0.02	107
3	5.0	4.60 ± 0.02	92
4	10.0	9.60 ± 0.03	96
5	15.0	14.70 ± 0.02	98

±: Standard deviation (n = 3)

deviation of the blank solution and m is the slope of the calibration curve,[60] resulting in an LOD of 0.47 nM. The sensitivity of the electrode was determined to be 0.0389 A M^{-1}. Table 1 compares the electrochemical DA sensing performance of various ZnO-based electrodes in aqueous solutions. While many ZnO-based composites offer enhanced sensing performance,[8,59–61] they often require complex synthesis methods and exhibit inconsistent material quality, affecting reliability and performance. In contrast, our single-metal oxide ZnO is simpler, more cost-effective, and easier to produce, ensuring better uniformity and consistent performance, with the results comparable to composite materials.[2,9,14,59,60] The enhanced electrochemical performance of the ZnO/GC electrode for DA oxidation may be attributed to the unique morphology of ZnO.

Different concentrations of DA solution were prepared using DA hydrochloride injection in 0.1 M PBS to represent real sample analysis. Recovery experiments were performed by differential pulse voltammetry using a standard three electrode system. The background current was corrected to precisely determine the recovery (%) of DA, and three sequential experiments were performed. The recovery amounts for DA ranged from 92 to 107% (Table 2), demonstrating the practical reliability of the proposed sensor.

4. Conclusions

We demonstrate a low-cost method for synthesizing uniquely leaf-shaped ZnO using metallic Zn shells obtained from waste batteries via precipitation. The ZnO/GC electrode detects dopamine (DA) in the range of 0.01 to 100 μM, with a low limit of detection of 0.47 nM, which is below the physiological concentration. The developed sensor shows promising DA selectivity even in the presence of interfering species and exhibits good reproducibility. Moreover, the proposed ZnO/GC electrode can detect DA in real samples. The affordability of the precursors for synthesizing leaf-shaped ZnO offers an economical electrochemical sensor for detecting DA and other potential biomolecules, while also promoting environmentally sustainable e-waste management.

Data availability

Data will be made available on request.

Conflicts of interest

There are no conflicts to declare.

References

1 S. S. J. Aravind and S. Ramaprabhu, Dopamine Biosensor with Metal Oxide Nanoparticles Decorated Multi-Walled Carbon Nanotubes, *Nanosci. Methods*, 2012, **1**(1), 102–114.

2 H. Y. Yue, H. J. Zhang, S. Huang, X. X. Lu, X. Gao, S. S. Song, Z. Wang, W. Q. Wang and E. H. Guan, Highly Sensitive and Selective Dopamine Biosensor Using Au Nanoparticles-ZnO Nanocone Arrays/Graphene Foam Electrode, *Mater. Sci. Eng., C*, 2020, **108**, 110490.

3 H. Y. Yue, H. J. Zhang, S. Huang, X. X. Lu, X. Gao, S. S. Song, Z. Wang, W. Q. Wang and E. H. Guan, Highly Sensitive and Selective Dopamine Biosensor Using Au Nanoparticles-ZnO Nanocone Arrays/Graphene Foam Electrode, *Mater. Sci. Eng., C*, 2020, **108**, 110490.

4 U. Ungerstedt; M. Herrera-Marschitz and T. Zetterström, Dopamine Neurotransmission and Brain Function, in *Progress in Brain Research*, ed. Buijs, R. M., Pévet, P., Swaab, D. F., Chemical Transmission in the Brain: The Role of Amines, Amino Acids and Peptides, Elsevier, 1982, vol. 55, pp. 41–49.

5 J. Birtwistle and D. Baldwin, Role of Dopamine in Schizophrenia and Parkinson's Disease, *Br. J. Nurs.*, 1998, **7**(14), 832–841.

6 J. Segura-Aguilar, I. Paris, P. Muñoz, E. Ferrari, L. Zecca and F. A. Zucca, Protective and Toxic Roles of Dopamine in Parkinson's Disease, *J. Neurochem.*, 2014, **129**(6), 898–915.

7 Mounesh, K. V. Reddy and O. Nagaraja, Novel *n*-octadecylcarboxamide CoPc: amperometric detections for bioanalytes using modified GCE, *Chem. Papers*, 2021, **75**, 2945–2956.

8 C. Nong, B. Yang, X. Li, S. Feng and H. Cui, Electrochemical Sensor Based on Three-Dimensional rGO/ZnO Composite for Dopamine Detection, *Int. J. Electrochem. Sci.*, 2022, **17**(3), 220331.

9 X. Zhang, Y.-C. Zhang and L.-X. Ma, One-Pot Facile Fabrication of Graphene-Zinc Oxide Composite and Its Enhanced Sensitivity for Simultaneous Electrochemical Detection of Ascorbic Acid, Dopamine and Uric Acid, *Sens. Actuators, B*, 2016, **227**, 488–496.

10 F. Li, B. Ni, Y. Zheng, Y. Huang and G. Li, A Simple and Efficient Voltammetric Sensor for Dopamine Determination Based on ZnO Nanorods/Electro-Reduced Graphene Oxide Composite, *Surf. Interfaces*, 2021, **26**, 101375.

11 M. Ni, J. Chen, C. Wang, Y. Wang, L. Huang, W. Xiong, P. Zhao, Y. Xie and J. Fei, A High-Sensitive Dopamine

Electrochemical Sensor Based on Multilayer Ti₃C₂ MXene, Graphitized Multi-Walled Carbon Nanotubes and ZnO Nanospheres, *Microchem. J.*, 2022, **178**, 107410.

12 D. Balram, K.-Y. Lian and N. Sebastian, A Novel Electrochemical Sensor Based on Flower Shaped Zinc Oxide Nanoparticles for the Efficient Detection of Dopamine, *Int. J. Electrochem. Sci.*, 2018, **13**(2), 1542–1555.

13 K. V. Reddy, Novel garnished cobalt (II) phthalocyanine with MWCNTs on modified GCE: sensitive and reliable electrochemical investigation of paracetamol and dopamine, *New J. Chem.*, 2020, **44**(39), 16831–16844.

14 C. Yang, C. Zhang, T. Huang, X. Dong and L. Hua, Ultra-Long ZnO/Carbon Nanofiber as Free-Standing Electrochemical Sensor for Dopamine in the Presence of Uric Acid, *J. Mater. Sci.*, 2019, **54**(24), 14897–14904.

15 B. S. Jilani, M. Pari, K. V. Reddy and K. S. Lokesh, Simultaneous and sensitive detection of ascorbic acid in presence of dopamine using MWCNTs-decorated cobalt (II) phthalocyanine modified GCE, *Microchem. J.*, 2019, **147**, 755–763.

16 R. F. Gibson, A Review of Recent Research on Mechanics of Multifunctional Composite Materials and Structures, *Compos. Struct.*, 2010, **92**(12), 2793–2810.

17 V. B. Mohan, K. Lau, D. Hui and D. Bhattacharyya, Graphene-Based Materials and Their Composites: A Review on Production, Applications and Product Limitations, *Composites, Part B*, 2018, **142**, 200–220.

18 Z. S. Campbell, S. Baro, Y. Gao, F. Li and M. Abolhasani, Flow Synthesis of Single and Mixed Metal Oxides, *Chem.:Methods*, 2022, **2**(8), e202200007.

19 T. P. Mabate, N. P. Maqunga, S. Ntshibongo, M. Maumela and N. Bingwa, Metal Oxides and Their Roles in Heterogeneous Catalysis: Special Emphasis on Synthesis Protocols, Intrinsic Properties, and Their Influence in Transfer Hydrogenation Reactions, *SN Appl. Sci.*, 2023, **5**(7), 196.

20 Y. Yoon, P. L. Truong, D. Lee and S. H. Ko, Metal-Oxide Nanomaterials Synthesis and Applications in Flexible and Wearable Sensors, *ACS Nanosci. Au*, 2022, **2**(2), 64–92.

21 K. Zhang, J. L. Schnoor and E. Y. Zeng, E-Waste Recycling: Where Does It Go from Here?, *Environ. Sci. Technol.*, 2012, **46**(20), 10861–10867.

22 E. Sanchez Moran, D. Prodius, I. C. Nlebedim and M. Mba Wright, Rare-Earth Elements Recovery from Electronic Waste: Techno-Economic and Life Cycle Analysis, *ACS Sustainable Chem. Eng.*, 2024, **12**(38), 14164–14172.

23 M. H. Kabir, M. Y. Pabel, N. T. Bristy, M. A. Salam, M. S. Bashar and S. Yasmin, From e-waste to eco-sensors: synthesis of reduced graphene oxide/ZnO from discarded batteries for a rapid electrochemical bisphenol A sensor, *RSC Adv.*, 2024, **14**(48), 36073–36083.

24 T. Zhang, B. Zhang, X. Bai, Y. Yao, L. Wang, Y. Shu, K. Kannan, X. Huang and H. Sun, Health Status of Elderly People Living Near E-Waste Recycling Sites: Association of E-Waste Dismantling Activities with Legacy Perfluoroalkyl Substances (PFASs), *Environ. Sci. Technol. Lett.*, 2019, **6**(3), 133–140.

25 M. Yan, Z. Cheng, Q. Zou, H. Zhao, L. Yang, H. Zhu, T. Zhang and H. Sun, Human Exposure Levels of Volatile Organic Compounds in E-Waste Recycling Area: Get Insight into Impacts of Manipulation Mode and Associations with Oxidative Stress Markers, *Environ. Health*, 2023, **1**(6), 405–415.

26 M. H. Kabir, M. J. Miah, A. K. Mohiuddin, M. S. Hossain, B. P. Upoma, M. A. A. Shaikh, M. Y. Pabel, F. Mojumder, R. Mahmud, N. I. Tanvir and S. Yasmin, Highly Effective Removal of Moxifloxacin from Aqueous Solutions Using Graphene Oxide Functionalized with Sodium Dodecyl Sulfate, *ACS Sustainable Resour. Manage.*, 2025, **2**(2), 256–266.

27 I. De Michelis, F. Ferella, E. Karakaya, F. Beolchini and F. Vegliò, Recovery of Zinc and Manganese from Alkaline and Zinc-Carbon Spent Batteries, *J. Power Sources*, 2007, **172**(2), 975–983.

28 M. Y. Pabel, S. Yasmin, M. A. A. Shaikh and M. H. Kabir, Electronic Waste Derived Reduced Graphene Oxide Supported Silver Nanoparticles for the Electrochemical Sensing of Trace Level Arsenite in Aqueous Medium, *Sens. Actuators, A*, 2024, **366**, 115028.

29 F. Mojumder, S. Yasmin, M. A. A. Shaikh, P. Chowdhury and M. H. Kabir, Synthesis of Reusable Graphene Oxide Based Nickel-Iron Superparamagnetic Nanoadsorbent from Electronic Waste for the Removal of Doxycycline in Aqueous Media, *J. Hazard. Mater. Adv.*, 2024, **14**, 100429.

30 Md. S. Hossain, S. Yasmin and M. H. Kabir, Cost-Effective Synthesis of Magnetic Graphene Oxide Nanocomposite from Waste Battery for the Removal of Arsenic from Aqueous Solutions: Adsorption Mechanism with DFT Calculation, *J. Saudi Chem. Soc.*, 2024, **28**(3), 101873.

31 S. Yasmin, M. G. Azam, M. S. Hossain, U. S. Akhtar and M. H. Kabir, Efficient Removal of Ciprofloxacin from Aqueous Solution Using Zn–C Battery Derived Graphene Oxide Enhanced by Hydrogen Bonding, Electrostatic and π–π Interaction, *Heliyon*, 2024, **10**(12), e33317.

32 M. H. Kabir, M. S. Hossain, M. M. Rahman, M. Ashrafuzzaman, M. Hasan, M. Y. Pabel, D. Islam, M. Shahriar Bashar, T. Faruque and S. Yasmin, Green Reduction of Waste-Battery-Derived Graphene Oxide by Jute Leaves and Its Application for the Removal of Tetracyclines from Aqueous Media, *ACS Sustainable Resour. Manage.*, 2024, **1**(8), 1812–1823.

33 M. Aliannezhadi, S. Z. Mirsanaee, M. Jamali and F. Shariatmadar Tehrani, The Physical Properties and Photocatalytic Activities of Green Synthesized ZnO Nanostructures Using Different Ginger Extract Concentrations, *Sci. Rep.*, 2024, **14**(1), 2035.

34 B. Naiel, M. Fawzy, M. W. A. Halmy and A. E. D. Mahmoud, Green Synthesis of Zinc Oxide Nanoparticles Using Sea Lavender (Limonium Pruinosum L. Chaz.) Extract: Characterization, Evaluation of Anti-Skin Cancer, Antimicrobial and Antioxidant Potentials, *Sci. Rep.*, 2022, **12**(1), 20370.

35 M. F. Ehsan, H. R. Barai, M. M. Islam, M. A. B. H. Susan, S. W. Joo and M. S. Miran, ZnO Nanocomposites Supported by Acid-Activated Kaolinite as Photocatalysts for the Enhanced Photodegradation of an Organic Dye, *Mater. Today Commun.*, 2023, **36**, 106563.

36 Md. A. Faisal, S. Ahmed and Md. A. B. H. Susan, Nanostructured ZnO with Tunable Morphology from Double-Salt Ionic Liquids as Soft Template, *ACS Omega*, 2024, **9**(11), 12992–13005.

37 M. Izzi, M. C. Sportelli, L. Torsi, R. A. Picca and N. Cioffi, Synthesis and Antimicrobial Applications of ZnO Nanostructures: A Review, *ACS Appl. Nano Mater.*, 2023, **6**(13), 10881–10902.

38 S. Maher, S. Nisar, S. M. Aslam, F. Saleem, F. Behlil, M. Imran, M. A. Assiri, A. Nouroz, N. Naheed, Z. A. Khan and P. Aslam, Synthesis and Characterization of ZnO Nanoparticles Derived from Biomass (Sisymbrium Irio) and Assessment of Potential Anticancer Activity, *ACS Omega*, 2023, **8**(18), 15920–15931.

39 S. V. Nistor, D. Ghica, M. Stefan, I. Vlaicu, J. N. Barascu and C. Bartha, Magnetic Defects in Crystalline Zn(OH)₂ and Nanocrystalline ZnO Resulting from Its Thermal Decomposition, *J. Alloys Compd.*, 2013, **548**, 222–227.

40 M. Ghaedi, H. Z. Khafri, A. Asfaram and A. Goudarzi, Response Surface Methodology Approach for Optimization of Adsorption of Janus Green B from Aqueous Solution onto ZnO/Zn(OH)₂-NP-AC: Kinetic and Isotherm Study, *Spectrochim. Acta, Part A*, 2016, **152**, 233–240.

41 V. Anand, A. Sakthivelu, K. D. A. Kumar, S. Valanarasu, V. Ganesh, M. Shkir, A. Kathalingam and S. AlFaify, Novel Rare Earth Gd and Al Co-Doped ZnO Thin Films Prepared by Nebulizer Spray Method for Optoelectronic Applications, *Superlattices Microstruct.*, 2018, **123**, 311–322.

42 L. Saikia, D. Bhuyan, M. Saikia, B. Malakar, D. K. Dutta and P. Sengupta, Photocatalytic Performance of ZnO Nanomaterials for Self Sensitized Degradation of Malachite Green Dye under Solar Light, *Appl. Catal., A*, 2015, **490**, 42–49.

43 A. J. Santhosam, K. Ravichandran, M. Shkir and M. Sridharan, Effect of La Incorporation on the NH3 Sensing Behaviour of ZnO Thin Films Prepared Using Low-Cost Nebulizer Spray Technique, *J. Mater. Sci. Mater. Electron.*, 2020, **31**(16), 13240–13248.

44 J. Tauc, Optical Properties of Amorphous Semiconductors, in *Amorphous and Liquid Semiconductors*, ed. Tauc, J., Springer, US, Boston, MA, 1974, pp. 159–220.

45 D. Ponnusamy and S. Madanagurusamy, Nanostructured ZnO Films for Room Temperature Ammonia Sensing, *J. Electron. Mater.*, 2014, **43**(9), 3211–3216.

46 H. F. Wilson, C. Tang and A. S. Barnard, Morphology of Zinc Oxide Nanoparticles and Nanowires: Role of Surface and Edge Energies, *J. Phys. Chem. C*, 2016, **120**(17), 9498–9505.

47 A. Sulciute, K. Nishimura, E. Gilshtein, F. Cesano, G. Viscardi, A. G. Nasibulin, Y. Ohno and S. Rackauskas, ZnO Nanostructures Application in Electrochemistry: Influence of Morphology, *J. Phys. Chem. C*, 2021, **125**(2), 1472–1482.

48 Q. C. Bui, G. Ardila, E. Sarigiannidou, H. Roussel, C. Jiménez, O. Chaix-Pluchery, Y. Guerfi, F. Bassani, F. Donatini, X. Mescot, B. Salem and V. Consonni, Morphology Transition of ZnO from Thin Film to Nanowires on Silicon and Its Correlated Enhanced Zinc Polarity Uniformity and Piezoelectric Responses, *ACS Appl. Mater. Interfaces*, 2020, **12**(26), 29583–29593.

49 L.-Y. Wang, B.-Y. Shi, C.-B. Yao, Z.-M. Wang, X. Wang, C.-H. Jiang, L.-F. Feng and Y.-L. Song, Size and Morphology

50 A. Rezaei, E. Katoueizadeh and S. M. Zebarjad, Investigation of the Parameters Affecting the Morphology of Zinc Oxide (ZnO) Nanoparticles Synthesized by Precipitation Method, *Mater. Today Chem.*, 2022, **26**, 101239.

51 L. Xu, Y. Guo, Q. Liao, J. Zhang and D. Xu, Morphological Control of ZnO Nanostructures by Electrodeposition, *J. Phys. Chem. B*, 2005, **109**(28), 13519–13522.

52 M. Søndergaard, E. D. Bøjesen, M. Christensen and B. B. Iversen, Size and Morphology Dependence of ZnO Nanoparticles Synthesized by a Fast Continuous Flow Hydrothermal Method, *Cryst. Growth Des.*, 2011, **11**(9), 4027–4033.

53 V. Ball, D. D. Frari, V. Toniazzo and D. Ruch, Kinetics of Polydopamine Film Deposition as a Function of pH and Dopamine Concentration: Insights in the Polydopamine Deposition Mechanism, *J. Colloid Interface Sci.*, 2012, **386**(1), 366–372.

54 T.-P. Chen, T. Liu, T.-L. Su and J. Liang, Self-Polymerization of Dopamine in Acidic Environments without Oxygen, *Langmuir*, 2017, **33**(23), 5863–5871.

55 X. Du, L. Li, F. Behboodi-Sadabad, A. Welle, J. Li, S. Heissler, H. Zhang, N. Plumeré and P. A. Levkin, Bio-Inspired Strategy for Controlled Dopamine Polymerization in Basic Solutions, *Polym. Chem.*, 2017, **8**(14), 2145–2151.

56 C. Zhu, H. Xie, Y. Zhang, R. Zhang, S. Dai, Y. Li, Y. Sun, Y. Zhang and M. Zhao, Exploring the Complex Impact of Proteins on Dopamine Polymerization: Mechanisms and Strategies for Modulation, *J. Phys. Chem. B*, 2024, **128**(12), 2885–2896.

57 Y. Yang, P. Qi, Y. Ding, M. F. Maitz, Z. Yang, Q. Tu, K. Xiong, Y. Leng and N. Huang, A Biocompatible and Functional Adhesive Amine-Rich Coating Based on Dopamine Polymerization, *J. Mater. Chem. B*, 2015, **3**(1), 72–81.

58 N. Delmo, B. Mostafiz, A. E. Ross, J. Suni and E. Peltola, Developing an Electrochemical Sensor for the in Vivo Measurements of Dopamine, *Sens. Diagn.*, 2023, **2**(3), 559–581.

59 S. Thareja and A. Kumar, In Situ Wet Synthesis of N-ZnO/N-rGO Nanohybrids as an Electrode Material for High-Performance Supercapacitors and Simultaneous Nonenzymatic Electrochemical Sensing of Ascorbic Acid, Dopamine, and Uric Acid at Their Interface, *J. Phys. Chem. C*, 2021, **125**(45), 24837–24848.

60 S. Ponnada, D. B. Gorle, M. S. Kiai, S. Rajagopal, R. K. Sharma and A. Nowduri, A Facile, Cost-Effective, Rapid, Single-Step Synthesis of Ag–Cu Decorated ZnO Nanoflower-like Composites (NFLCs) for Electrochemical Sensing of Dopamine, *Mater. Adv.*, 2021, **2**(18), 5986–5996.

61 R. Appiah-Ntiamoah, A. F. Baye and H. Kim, ZnO–ZnFe₂O₄/Fe₃O₄/Carbon Nanocomposites for Ultrasensitive and Selective Dopamine Detection, *ACS Appl. Nano Mater.*, 2022, **5**(4), 4754–4766.

62 H. Teymourian, A. Barfidokht and J. Wang, Electrochemical Glucose Sensors in Diabetes Management: An Updated

Review (2010–2020), *Chem. Soc. Rev.*, 2020, **49**(21), 7671–7709.

63 Z. Haghparas, Z. Kordrostami, M. Sorouri, M. Rajabzadeh and R. Khalifeh, Highly Sensitive Non-Enzymatic Electrochemical Glucose Sensor Based on Dumbbell-Shaped Double-Shelled Hollow Nanoporous CuO/ZnO Microstructures, *Sci. Rep.*, 2021, **11**(1), 344.

64 S. Yasmin, M. S. Ahmed, D. Park and S. Jeon, Nitrogen-Doped Graphene Supported Cobalt Oxide for Sensitive Determination of Dopamine in Presence of High Level Ascorbic Acid, *J. Electrochem. Soc.*, 2016, **163**(9), B491.

65 N. Roy, S. Yasmin and S. Jeon, Effective Electrochemical Detection of Dopamine with Highly Active Molybdenum Oxide Nanoparticles Decorated on 2, 6 Diaminopyridine/Reduced Graphene Oxide, *Microchem. J.*, 2020, **153**, 104501.

66 S. Yasmin, M. S. Ahmed and S. Jeon, Determination of Dopamine by Dual Doped Graphene-Fe_2O_3 in Presence of Ascorbic Acid, *J. Electrochem. Soc.*, 2015, **162**(14), B363.

67 Y. Tang, R. Huang, C. Liu, S. Yang, Z. Lu and S. Luo, Electrochemical Detection of 4-Nitrophenol Based on a Glassy Carbon Electrode Modified with a Reduced Graphene Oxide/Au Nanoparticle Composite, *Anal. Methods*, 2013, **5**(20), 5508–5514.

68 A. M. Visagamani, M. Harb, K. Kaviyarasu, A. Muthukrishnaraj, M. Ayyar, K. A. Alzahrani, R. H. Althomali and S. A. Althobaiti, Electrochemical Detection of 4-Nitrophenol Using a Novel $SrTiO_3$/Ag/rGO Composite, *ACS Omega*, 2023, **8**(45), 42479–42491.

69 A. K. Mohiuddin, S. Yasmin and S. Jeon, Co_xNi_{1-x} Double Hydroxide Decorated Graphene NPs for Simultaneous

Determination of Dopamine and Uric Acid, *Sens. Actuators, A*, 2023, **355**, 114314.

70 S. Masrat, V. Nagal, M. Khan, A. Ahmad, M. B. Alshammari, S. Alam, U. T. Nakate, B. Lee, P. Mishra, K. S. Bhat and R. Ahmad, Electrochemical Sensing of Uric Acid with Zinc Oxide Nanorods Decorated with Copper Oxide Nanoseeds, *ACS Appl. Nano Mater.*, 2023, **6**(18), 16615–16624.

71 O. E. Fayemi, R. Baskar, A. S. Adekunle, E.-S. M. Sherif and E. E. Ebenso, SPEEK/ZnO Nanocomposite Modified Gold Electrode for Electrochemical Detection of Dopamine, *Electroanalysis*, 2020, **32**(12), 2713–2722.

72 T. G. Beatto, W. E. Gomes, A. Etchegaray, R. Gupta and R. K. Mendes, Dopamine Levels Determined in Synthetic Urine Using an Electrochemical Tyrosinase Biosensor Based on ZnO@Au Core–Shell, *RSC Adv.*, 2023, **13**(47), 33424–33429.

73 Y. Li, M. Xie, X. Kang, W. Hou and Y. Chen, Preparation of Rod-Zinc Oxide/Agaric Derived Porous Carbon Nanocomposites and Their Application in Electrochemical Sensing, *New J. Chem.*, 2024, **48**(37), 16289–16296.

74 M. E. Guye, F. K. Egualle, R. Appiah-Ntiamoah, S. K. Kassahun and H. Kim, Synergetic Effect of Optimized β-$Zn(OH)_2$/ZnO Heterostructure towards Electrochemical Dopamine Detection, *J. Alloys Compd.*, 2024, **1002**, 175184.

75 J. Ahmed, M. Faisal, J. S. Algethami, M. Alsaiari and F. A. Harraz, A Novel In_2O_3-Doped ZnO Decorated Mesoporous Carbon Nanocomposite as a Sensitive and Selective Dopamine Electrochemical Sensor, *J. Mater. Res. Technol.*, 2024, **29**, 540–549.